Nanoscale Advances

PAPER

View Article Online
View Journal | View Issue

Cite this: *Nanoscale Adv.*, 2019, **1**, 1980

Epitaxial highly ordered Sb:SnO_2 nanowires grown by the vapor liquid solid mechanism on m-, r- and a-Al_2O_3†

M. Zervos, *[a] N. Lathiotakis, [b] N. Kelaidis,[c] A. Othonos,[d] E. Tanasa[e] and E. Vasile[e]

Epitaxial, highly ordered Sb:SnO_2 nanowires were grown by the vapor–liquid–solid mechanism on m-, r- and a-Al_2O_3 between 700 °C and 1000 °C using metallic Sn and Sb with a mass ratio of Sn/Sb = 0.15 ± 0.05 under a flow of Ar and O_2 at 1 ± 0.5 mbar. We find that effective doping and ordering can only be achieved inside this narrow window of growth conditions. The Sb:SnO_2 nanowires have the tetragonal rutile crystal structure and are inclined along two mutually perpendicular directions forming a rectangular mesh on m-Al_2O_3 while those on r-Al_2O_3 are oriented in one direction. The growth directions do not change by varying the growth temperature between 700 °C and 1000 °C but the carrier density decreased from 8×10^{19} cm^{-3} to 4×10^{17} cm^{-3} due to the re-evaporation and limited incorporation of Sb donor impurities in SnO_2. The Sb:SnO_2 nanowires on r-Al_2O_3 had an optical transmission of 80% above 800 nm and displayed very long photoluminescence lifetimes of 0.2 ms at 300 K. We show that selective area location growth of highly ordered Sb:SnO_2 nanowires is possible by patterning the catalyst which is important for the realization of novel nanoscale devices such as nanowire solar cells.

Received 7th February 2019
Accepted 9th April 2019

DOI: 10.1039/c9na00074g

rsc.li/nanoscale-advances

1 Introduction

Metal oxide semiconductor nanowires (NWs) such as Sb:SnO_2,[1] Sn:In_2O_3,[2] Al:ZnO[3] and In:ZnO[4] NWs have a high conductivity but they are also capable of light emission as shown for Sn:In_2O_3 NWs by O' Dwyer *et al.*[5] and Gao *et al.*[6] Despite ongoing efforts into the growth and properties of such metal oxide (MO) NWs only a few have obtained epitaxial, ordered networks which is essential for the realization of novel nanoscale devices with improved performance like nanowire solar cells (NWSCs). More specifically Wan *et al.*[7] has obtained ordered Sn :In_2O_3 NWs by homo epitaxy on an Sn:In_2O_3 buffer layer while Nguyen *et al.*[8] and Gao *et al.*[6] have obtained ordered Sn:In_2O_3 NWs by hetero epitaxy on m-, a- and c-Al_2O_3. To the best of our knowledge all other MO NWs that have been obtained previously are not oriented in an epitaxial fashion along any particular direction. It is important then to obtain earth abundant MO NWs such as Sb:SnO_2 NWs as low cost alternatives to Sn:In_2O_3.

In the past we have grown SnO_2 NWs *via* the vapor liquid solid (VLS) mechanism at 800 °C and 10^{-1} mbar which had a carrier density of the order of 10^{16} cm^{-3} and mobility of 70 cm^2 V^{-1} s^{-1}, as determined from THz conductivity spectroscopy.[9] High conductivity SnO_2 NWs have been obtained *via* the incorporation of Sb,[10] Mo[11] and F[12] in SnO_2 NWs, while recently, Ma *et al.*[13] showed theoretically that a semiconductor to semimetal transition is possible *via* the incorporation of Pb in SnO_2. However, in most cases Sb has been used as an n-type donor impurity in SnO_2 NWs.[14–24] All of the Sb:SnO_2 NWs have been obtained by using metallic Sn and Sb in the past, but they were not ordered.

Nevertheless, it is necessary to point out that Mathur *et al.*[25] has obtained un-doped SnO_2 NWs *via* the VLS mechanism that were ordered on TiO_2 (001) which is isostructural with the tetragonal rutile crystal structure of SnO_2. Similarly, Kim *et al.*[26] obtained un-doped, epitaxial, SnO_2 NWs on TiO_2 (101) while Leonardy *et al.*[27] investigated the structural properties of ordered, un-doped, SnO_2 NWs on m- and a-Al_2O_3 at 700 °C by using SnO under a flow of Ar at 10 mbar. Both Mathur *et al.*[25] and Leonardy *et al.*[27] obtained SnO_2 NWs which were oriented in two mutually perpendicular directions while the SnO_2 NWs of Kim *et al.*[26] were aligned in three directions. Others like Mazeina *et al.*[28] have grown vertical, un-doped SnO_2 NWs *via* the VLS mechanism on c-Al_2O_3 at 900 °C with limited ordering and

[a]*Nanostructured Materials and Devices Laboratory, School of Engineering, University of Cyprus, PO Box 20537, Nicosia, 1678, Cyprus. E-mail: zervos@ucy.ac.cy*
[b]*Theoretical and Physical Chemistry Institute, National Hellenic Research Foundation, Vass. Constantinou 48, GR-11635 Athens, Greece*
[c]*Faculty of Engineering, Environment and Computing, Coventry University, Priory Street, Coventry CV1 5FB, UK*
[d]*Laboratory of Ultrafast Science, Department of Physics, University of Cyprus, P.O. Box 20537, Nicosia, 1678, Cyprus*
[e]*Department of Science and Engineering of Oxide Materials and Nanomaterials, Politehnica University of Bucharest, 313 Splaiul Independentei, Bucharest, 060042, Romania*

† Electronic supplementary information (ESI) available. See DOI: 10.1039/c9na00074g

uniformity. Lateral, but un-doped SnO_2 NWs have also been obtained by Kim *et al.*[29] and Choi *et al.*[30] while more recently Wang *et al.*[31] investigated lateral SnO_2 NWs that were aligned on the surface of m-Al_2O_3. All of these studies on epitaxial, ordered un-doped SnO_2 NWs[25–30] focused primarily on their growth and structural properties. It is imperative then to investigate the electrical and optical properties of similar Sb:SnO_2 NWs which is critical in evaluating their potential for subsequent use in devices such as NWSCs.

Here we show that epitaxial, ordered Sb:SnO_2 NWs can be grown *via* the VLS mechanism on m-, r- and a- oriented Al_2O_3 only in a narrow window of growth conditions. We describe their morphology, structural, electrical and optical properties, in detail and show that selective area location growth of ordered Sb:SnO_2 NWs is possible which in turn is attractive for the realization of NWSCs as a low cost alternative to Sn:In_2O_3 NWs.

2 Methods

2.1. Epitaxial growth of Sb:SnO_2 NWs

The Sb:SnO_2 NWs were grown using a 1″ hot wall, low pressure chemical vapour deposition (LPCVD) reactor, capable of reaching 1100 °C, which was fed *via* a micro flow leak valve positioned on the upstream side, just after the gas manifold which consists of four mass flow controllers. A chemically resistant, rotary pump that can reach 10^{-4} mbar was connected downstream. For the growth of the Sb:SnO_2 NWs, metallic Sn and Sb (Aldrich, 100 Mesh, 99.9%) were weighed with an accuracy of ±1 mg. We used an excess of Sb, *i.e.* a mass ratio of Sn/Sb ≈ 0.1, and the total mass of Sb and Sn was kept fixed and equal to 100 mg or 0.1 g. Square samples of 10 mm × 10 mm c-, m-, r- and a-Al_2O_3 were cleaned sequentially in trichloroethylene, methanol, acetone, isopropanol, rinsed with de-ionised water, dried with nitrogen and then coated with ≈1 nm Au. The elemental Sb and Sn as well as the c-, m-, r- or a-Al_2O_3 substrates were loaded in the same quartz boat which was positioned at the centre of the 1″ LPCVD reactor. The latter was pumped down to 10^{-4} mbar and purged with 1000 sccm of Ar for 10 min at 1 mbar. Subsequently the temperature was ramped up to 800 °C at 30°C min^{-1} using the same flow of Ar. Upon reaching 800 °C a flow of 10 sccm O_2 was added to the flow of Ar in order to grow the Sb:SnO_2 NWs over 10 min at 1 mbar, followed by cool down without O_2. We have grown Sb:SnO_2 NWs on c-, m-, r- and a-Al_2O_3 using these growth conditions and changed the growth temperature between 700 °C to 1000 °C.

2.2. Characterization of Sb:SnO_2 NWs

The morphology, crystal structure and composition of the Sb:SnO_2 NWs was determined by scanning electron microscopy (SEM), X-ray diffraction (XRD) and Energy Dispersive X-ray analysis (EDX). High resolution transmission electron microscopy (HRTEM) was carried out using a TECNAI F30 G^2 S-TWIN operated at 300 kV. The optical properties of the Sb:SnO_2 NWs were determined by steady state and transient absorption–transmission spectroscopy. The steady state and time resolved photoluminescence (PL) were also measured between 10 K and 300 K, while the electrical properties, *i.e.* carrier density and resistivity, were measured by the Hall effect in the Van der Pauw geometry similar to Costa *et al.*[23,24] In particular the Sb:SnO_2 NWs were transferred from the m-, r- or a-Al_2O_3 onto 10 mm × 10 mm c-Al_2O_3 by applying pressure. This results into a dry transfer of the ordered Sb:SnO_2 NWs onto the c-Al_2O_3 and the formation of a planar interconnected network. We then deposited In contacts over the Sb:SnO_2 NWs by thermal evaporation using a shadow mask. The Sb:SnO_2 NWs on c-Al_2O_3 was not heated up during the deposition, and the In contacts had diameters of ≈1 mm at the four corners of the 10 mm × 10 mm c-Al_2O_3, but we did not anneal them. The Hall effect was measured using a GMW3470 Electromagnet at 0.3 Tesla. The magnetic field was calibrated with a Hirst GM08 Gaussmeter. A Keithley 2635 A current source and Keithley 2182A nanovoltmeter, controlled by Lab View were used to provide a current and measure the voltages.

3 Results and discussion

In the past, we have shown that the reaction of Sn with O_2 at 800 °C and 10^{-1} mbar results into a high yield and uniform distribution of SnO_2 NWs on Si (001) or fused SiO_2. The SnO_2 NWs have average diameters of ≈50 nm, lengths up to ≈100 μm and grow by the VLS mechanism whereby Sn enters the Au catalyst particles on the surface of Si (001) or fused SiO_2 and forms liquid Au:Sn particles. Upon saturation, solid SnO_2 forms beneath the liquid Au:Sn particles *via* the reaction with O_2 at the triple phase junction, as shown in Fig. 1(a), leading to one dimensional, bottom-up growth.[32] However, the SnO_2 NWs obtained on Si (001) or fused SiO_2 were not oriented or ordered along any direction, and had a carrier density of the order of 10^{16} cm^{-3} with a mobility of 70 cm^2 V^{-1} s^{-1}, as determined from THz conductivity spectroscopy.[33] Hence doping is required to increase their conductivity. Recently, we showed that higher carrier densities of the order of 10^{18} to 10^{19} cm^{-3} may be readily obtained in Sb doped SnO_2 NWs grown on both Si (001) and fused SiO_2.[34] We obtained a high carrier density of 4 × 10^{19} cm^{-3} in the Sb:SnO_2 NWs grown on c-Al_2O_3 at 800 °C and 1 mbar by adding metallic Sb to Sn but the Sb:SnO_2 NWs were not ordered or oriented in any particular direction, similar to those obtained previously on Si (001) and fused SiO_2.[34] This is in contrast to the findings of Mazeina *et al.*,[28] who obtained vertical but un-doped SnO_2 NWs *via* the VLS mechanism on c-Al_2O_3 at 900 °C with a limited degree of ordering and uniformity. Similarly, we did not obtain ordered Sb:SnO_2 NWs on c-Al_2O_3 by changing the growth temperature between 800 °C and 1000 °C. The epitaxial growth and ordering of Sb:SnO_2 NWs on c-Al_2O_3 is not favorable in view of the fact that SnO_2 has a tetragonal crystal structure which will not match the hexagonal crystal structure of the underlying c-Al_2O_3. However, we observed the formation of ordered Sb:SnO_2 NWs on the sides of the c-Al_2O_3, as described in more detail in the ESI,† which is related to its specific crystallographic orientation. Therefore we carried out the growth of the Sb:SnO_2 NWs on m- , r- and a-Al_2O_3 at 800 °C and 1 mbar using the same growth conditions described above.

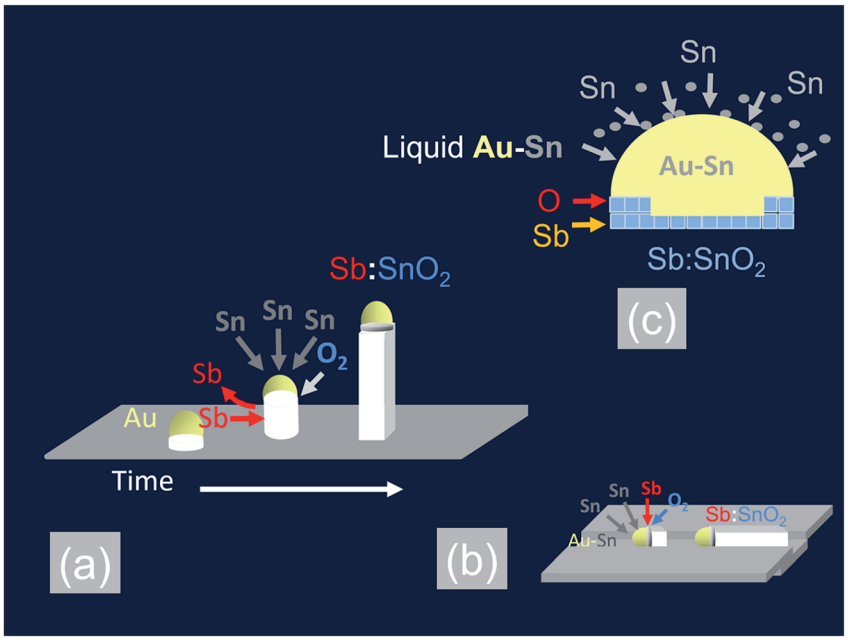

Fig. 1 Schematic representation of the VLS growth mechanism of $Sb:SnO_2$ NWs (a) bottom-up growth (b) lateral growth along a step or groove (c) Sb donor impurity incorporation mechanism.

3.1 Growth of $Sb:SnO_2$ NWs on m-, r- and a-Al_2O_3

We readily obtained ordered $Sb:SnO_2$ NWs on all three surfaces *i.e.* m-, r- and a-Al_2O_3, as shown in Fig. 2, 3 and 4 respectively. The $Sb:SnO_2$ NWs on m-Al_2O_3 are aligned along two mutually perpendicular directions as shown by the SEM images in Fig. 2(a and b), but are inclined with respect to the surface, similar to the SnO_2 NWs obtained by Mathur *et al.*[25] and Leonardy *et al.*[27] In contrast, the $Sb:SnO_2$ NWs on r-Al_2O_3 are all oriented along one direction as shown in Fig. 3(a)–(c). However, upon closer inspection we find that the $Sb:SnO_2$ NWs on r-Al_2O_3 consist of two segments. The first segment is inclined at $\theta = 68°$ and the second segment is at an angle of $\theta = 89°$, *i.e.* nearly perpendicular to the first, as shown in Fig. 3(f). This has also been observed by Jean *et al.*[20] who obtained $Sb:SnO_2$ NWs on 10 nm Au/Si (001) *via* the VLS mechanism at 1000 °C and 1 mbar using Sn/Sb = 50, 25 and 10 under Ar and trace amount of O_2,

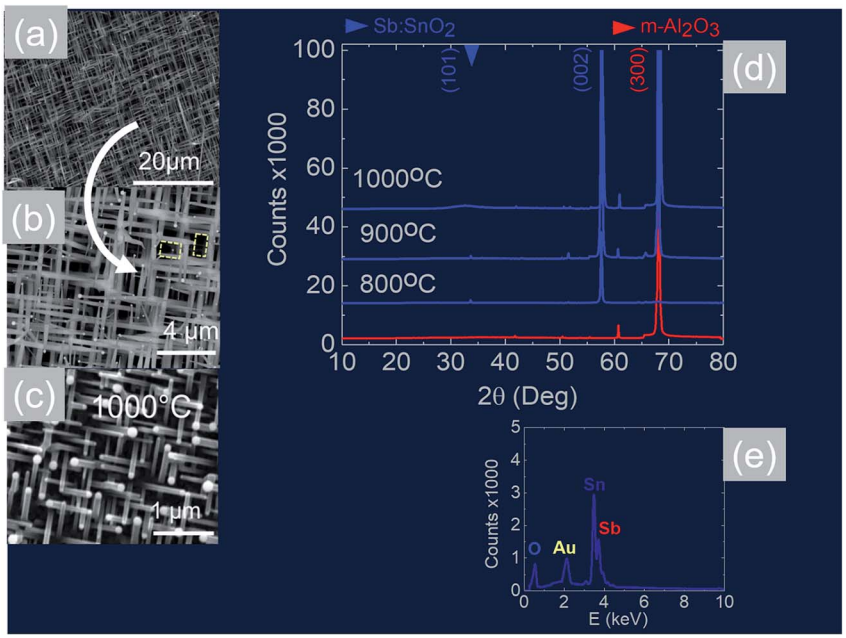

Fig. 2 SEM images of the $Sb:SnO_2$ NWs obtained at (a), (b) 800 °C and (c) 1000 °C on m-Al_2O_3 (d) XRD of m-Al_2O_3 (red) and $Sb:SnO_2$ NWs (blue) grown on m-Al_2O_3 at 800 °C, 900 °C and 1000 °C (e) EDX of the $Sb:SnO_2$ NWs.

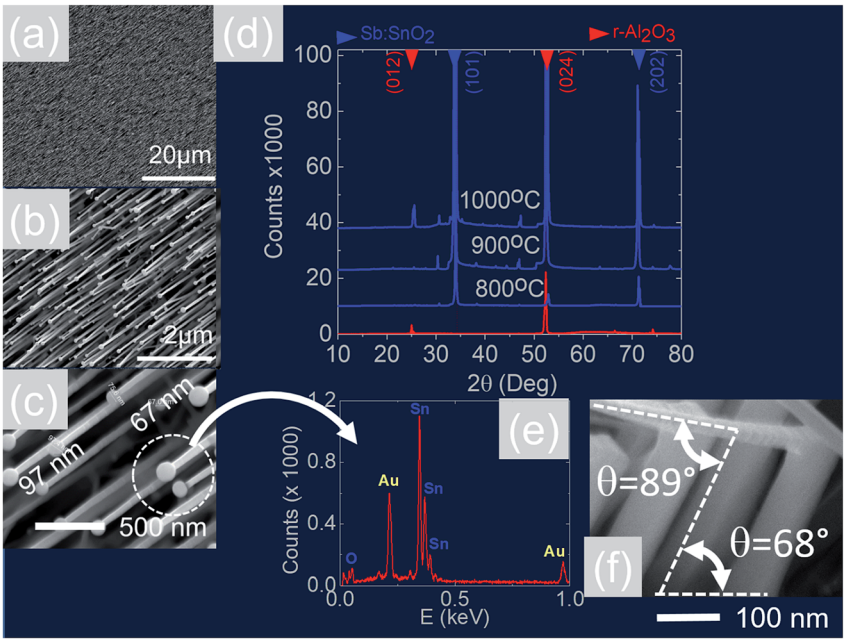

Fig. 3 (a)–(c) SEM images of the Sb:SnO_2 NWs obtained at 800 °C on r-Al_2O_3 (d) XRD of r-Al_2O_3 and Sb:SnO_2 NWs grown at 800 °C , 900 °C and 1000 °C (e) EDX of an Au:Sn particle on the end of a Sb:SnO_2 NW (f) side view showing that the first segment of the Sb:SnO_2 NWs grows at $\theta = 68°$ and the second segment at $\theta = 89°$ with respect to the first.

but their Sb:SnO_2 NWs were not aligned in any particular direction. The formation of the second segment can be prevented by reducing the growth time as will be described in more detail later. Similarly we find that the Sb:SnO_2 NWs on a-Al_2O_3 shown in Fig. 4(a–c) consist of two segments, similar to those obtained on r-Al_2O_3.

In all cases, we obtained a uniform distribution and ordering of Sb:SnO_2 NWs over the 10 mm × 10 m-, r- and a-Al_2O_3 in reproducible way, using Sn/Sb = 0.1 at 800 °C and 1 mbar as described above. Subsequently we varied the growth temperature between 700 °C to 1000 °C in order to find if any changes occur in the growth directions and ordering. The Sb:SnO_2 NWs obtained at 900 °C on m-Al_2O_3 were very similar to those obtained at 800 °C, but we find that the Sb:SnO_2 NWs obtained at 1000 °C are short, as shown in Fig. 2(c), due to the fact that the Sn and Sb are more or less completely transferred into the gas stream under the flow of Ar during the temperature ramp, before the onset of one dimensional growth. In fact, the depletion of Sb during the temperature ramp is more significant than Sn, due to the fact that Sn has a melting point of 232 °C and

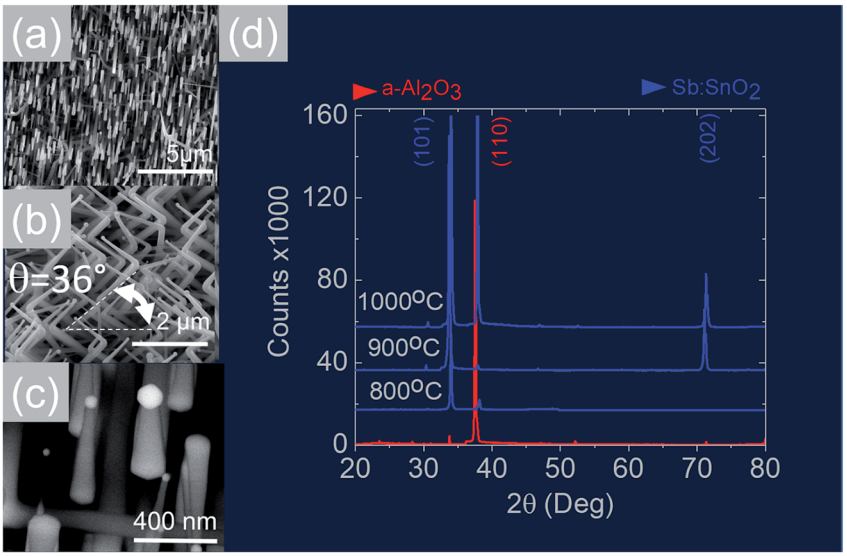

Fig. 4 (a)–(c) SEM images of the Sb:SnO_2 NWs obtained at 800 °C on a-Al_2O_3 (d) XRD of a-Al_2O_3 (red) and Sb:SnO_2 NWs (blue) grown on a-Al_2O_3 at 800 °C, 900 °C and 1000 °C.

vapor pressure of 10^{-5} mbar, while Sb has a higher melting point of 630 °C, but a remarkably higher vapor pressure of 10^{-1} mbar at 1000 °C. This in turn implies an important doping limitation when trying to obtain high carrier densities and conductivity in Sb:SnO_2 NWs using metallic Sn and Sb.[34] Likewise, the Sb:SnO_2 NWs obtained on m-Al_2O_3 at 700 °C were short, similar to those obtained at 1000 °C, due to the limited supply of Sn which has a lower vapor pressure at 700 °C, but they remained orthogonally oriented to each other. No changes occurred in the morphology and growth directions of the Sb:SnO_2 NWs on r- and a-Al_2O_3 by varying the temperature between 700 °C and 1000 °C. In contrast, the epitaxial growth and ordering of the Sb:SnO_2 NWs was critically dependent on the mass ratio of Sn/Sb. We obtained ordered Sb:SnO_2 NWs on m-, r- and a-Al_2O_3 only for Sn/Sb = 0.15 ± 0.05. One dimensional growth was completely suppressed when Sn/Sb < 0.1, and the Sb:SnO_2 NWs were not oriented in any particular direction for Sn/Sb > 0.2. Before elaborating further, it is important to mention that we did not obtain any Sb:SnO_2 NWs at all without adding O_2 to the flow of Ar during the growth step. In other words, the residual or background O_2 after purging and the temperature ramp was not significant, and the growth of the Sb:SnO_2 NWs occurred solely due to the oxygen supplied during the growth step.

Consequently the suppression of one dimensional growth for Sn/Sb < 0.1 is attributed to the total depletion and transfer of Sn into the gas stream during the temperature ramp, before the onset of growth, as it forms a liquid alloy with Sb. Note also that we did not obtain any SbO_2, Sb_2O_3 or Sb_2O_5 NWs by using only Sb.

On the other hand the Sb:SnO_2 NWs were not oriented in any particular direction for Sn/Sb > 0.2. From the above it is clear that an excess of Sb mixed with Sn provides flexible control over the Sn supplied to the Au particles which must be carefully tuned to a minimum for epitaxial growth and ordering to occur. This is further corroborated by the fact that we did not obtain ordered Sb:SnO_2 NWs without mixing the Sb and Sn even when Sn/Sb ≈ 0.15 ± 0.05.

In addition to the above it is important to point out that the epitaxial growth and ordering of the Sb:SnO_2 NWs also depends critically on the crystal quality of the m, r and a-Al_2O_3 surfaces. It has been shown that m-Al_2O_3 is thermodynamically unstable during high-temperature growth and nanostructured grooves composed of s- and r-facets develop along the [11$\bar{2}$0] direction.[35] In contrast Wang *et al.*[31] claimed that both the a- and r-plane of Al_2O_3 retain their surface structure at elevated temperatures. We annealed the m-, r- and a-Al_2O_3 at 1000 °C for 30 min under Ar and O_2 without any Sn, Sb or Au and observed a drastic reduction in the strength of the XRD peaks of the m- and a-Al_2O_3 but the r-Al_2O_3 appeared to maintain its surface crystallinity. Subsequently we deposited 1 nm of Au over the pre-annealed m-, r- and a-Al_2O_3 and tried to grow epitaxial, ordered Sb:SnO_2 NWs at 800 °C and 1 mbar using Sn/Sb = 0.1. As expected, we obtained ordered Sb:SnO_2 only on r-Al_2O_3. It appears then, that the deposition of 1 nm Au over pristine m-, r-, and a-Al_2O_3 at room temperature, prevents in some way the deterioration of the surface crystal structure and allows the epitaxial growth of ordered Sb:SnO_2 NWs at elevated temperatures between 700 °C to 1000 °C. In fact, the deposition of a 1 nm Au layer on the m-, r-, and a-Al_2O_3, which contain grooves or steps along specific crystallographic directions, leads to instabilities and ruptures of the Au at elevated temperatures as described by Hughes *et al.*[36] These ruptures occur at high curvature sites, *i.e.*, peaks and ridges, which act as retracting edges leading to a net flux of atoms away from the high positive curvature regions. For sufficiently thin layers, this process exposes the texture or steps of the underlying substrate, and a self-assembly of the Au particles will occur along specific crystallographic orientations.[37] This in turn will instigate one dimensional epitaxial growth along specific lateral crystallographic directions *via* the VLS mechanism, as shown in Fig. 1(b). When Sn is added to the Au particles, it is expected to reduce the surface tension and contact angle θ with the underlying m-, r- and a-Al_2O_3 surface, as a consequence of the fact that Sn and Sb have surface tensions of ≈500 mN m^{-1} and 350 mN m^{-1} respectively, but the surface tension of Au is ≈1000 mN m^{-1}. A large contact angle implies that the contact area is small, and *vice versa*, a smaller contact angle implies a larger contact area. Consequently, an excess of Sn is expected to lead to the formation of Au–Sn particles having a small contact angle and larger contact area with the underlying m, r and a-Al_2O_3 surface, in which case they might not be able to follow the variations in the surface topography which is necessary to obtain ordered Sb:SnO_2 NWs. The formation of ordered Sb:SnO_2 NWs is possible due to a reduction of the Sn by the excess of Sb during the temperature ramp, which in turn results into sufficiently small Au–Sn liquid particles that are able to follow steps or grooves on the surface during the growth step at elevated temperatures. Epitaxial growth, then, commences laterally, after which a transition to inclined growth occurs leading to the formation of the ordered networks of Sb:SnO_2 NWs shown in Fig. 2, 3 and 4.

All of the Sb:SnO_2 NWs on m-, r- and a-Al_2O_3 exhibited clear and well resolved peaks in the XRD, as shown in Fig. 2(d), 3(d) and 4(d) respectively, corresponding to the tetragonal rutile crystal structure of SnO_2. For comparison, we have included the XRD of the m-, r- and a-Al_2O_3 without the Sb:SnO_2 NWs. More specifically, the Sb:SnO_2 NWs on m-, r- and a-Al_2O_3 exhibit only one or two major peaks in their XRD, consistent with the fact that they grow along specific crystallographic directions. In contrast, we observed a multitude of major peaks from the Sb:SnO_2 NWs on c-Al_2O_3, due to the fact that they do not grow in an epitaxial fashion along specific directions, see ESI.† We did not observe any peaks related to oxides of Sb such as Sb_2O_3 or Sb_2O_5 which have melting points of 656 °C and 380 °C respectively. In addition, we do not observe any peaks suggesting the formation of Sb_2O_4, *i.e.* SbO_2 which is known to break down into Sb and O_2 at a higher temperature of 930 °C. Nevertheless the Sb:SnO_2 NWs contain Sb donor impurities as shown by the EDX spectrum in Fig. 2(e) and as confirmed previously by Raman spectroscopy.[34] Small differences in the amount of metallic Sb, *i.e.* for Sn/Sb = 0.15 ± 0.05, did not change the crystal structure or orientation of the Sb:SnO_2 NWs. We obtained exactly the same XRD spectra shown in Fig. 2, 3 and 4 for Sn/Sb = 0.1 and Sn/Sb = 0.15. However, it is important to point out that we did not detect any Sb in the Au particles on the ends of the Sb:SnO_2 NWs, as shown by the EDX spectrum in Fig. 3(e). This is consistent with the fact that we did not find Sb in the Au after

trying to grow Sb_2O_3, Sb_2O_5 or SbO_2 NWs, using just Sb, and leads us to suggest that the Sb donor impurities are incorporated into the SnO_2 NWs by surface diffusion, from their sides, as depicted in Fig. 1(c).

Now, the Sb:SnO_2 NWs on m-Al_2O_3 exhibited one dominant peak in the XRD, as shown in Fig. 2(d), corresponding to the (002), *i.e.* a multiple of (001), crystallographic planes of tetragonal rutile SnO_2. The two dimensional lattice of (001) SnO_2 and the oxygen terminated surface of m-Al_2O_3 are shown in Fig. 5(a) and (b) respectively. These have a small lattice mismatch of 0.5% so the Sb:SnO_2 NWs grow by a stacking of (001) planes on m-Al_2O_3 and the in-plane epitaxial relationship is SnO_2 (001)‖m-Al_2O_3. The growth of the Sb:SnO_2 NWs on m-Al_2O_3 is identical to that of SnO_2 NWs obtained by Leonardy *et al.*[27] on m-Al_2O_3 using SnO as opposed to Sn. For completeness, the tetragonal unit cell of SnO_2 is shown in Fig. 5(c), from which one may observe that the (101) crystallographic plane of SnO_2 is inclined at $\theta = 34°$ with respect to the (001). The Sb:SnO_2 NWs have rectangular sections, as shown in Fig. 5(d), and grow along the [101] crystallographic direction as confirmed by the HRTEM image of Fig. 5(e). Hence the Sb:SnO_2 NWs are inclined at $\theta = 34°$ with respect to the surface of m-Al_2O_3, and the fourth fold symmetry of the m-Al_2O_3 surface lattice gives rise to Sb:SnO_2 NWs oriented along two mutually orthogonal directions and the formation of the mesh structure observed in Fig. 2(a)–(c). This has also been confirmed by Wang *et al.*[31] who showed that un-doped SnO_2 NWs also grow laterally along two perpendicular directions and cross each other on m-Al_2O_3.

In contrast to the above we find that the Sb:SnO_2 NWs on r-Al_2O_3 exhibited two dominant peaks in the XRD, as shown in Fig. 3(d), corresponding to the (101) and (202) crystallographic planes of tetragonal rutile SnO_2. The two dimensional lattice of (101) SnO_2 and the oxygen terminated surface of r-Al_2O_3 are shown in Fig. 6(a) and (b) respectively. These have a larger lattice mismatch of 11%, and the in-plane epitaxial relationship is SnO_2 (101)‖r-Al_2O_3. The growth of the Sb:SnO_2 NWs on r-Al_2O_3 is very similar to the un-doped SnO_2 NWs of Kim *et al.*[38] which were also inclined at $\theta = 68°$ on r-Al_2O_3. Lateral SnO_2 NWs have also been obtained *via* the VLS mechanism by Kim *et al.*[29] on r-Al_2O_3 using C and SnO_2 as opposed to Sn but they did not observe the transition of growth from lateral to vertical SnO_2 NWs.

3.2 Selective area location growth of Sb:SnO_2 NWs on r-Al_2O_3

The VLS growth mechanism permits selective area location growth on m-, r- and a-Al_2O_3 as we did not obtain any Sb:SnO_2 NWs without using Au. We obtained hexagonally ordered Sb:SnO_2 NWs on r-Al_2O_3 by drop casting ~10 μl of 9 μm diameter polystyrene spheres on r-Al_2O_3, followed by the deposition of a thin layer of ~1 nm Au as shown in Fig. 7. Subsequently, the spheres were removed in isopropanol by ultrasonic vibration for 1 min, and the Sb:SnO_2 NWs were grown on the patterned Au on r-Al_2O_3 at 800 °C. The Sb:SnO_2 NWs on r-Al_2O_3 do not consist of two segments due to the reduced growth time. One may clearly observe that the Sb:SnO_2 NWs grow on the r-Al_2O_3 in a hexagonal pattern suggesting that one may also obtain different geometries in order to tailor the absorption–transmission spectrum in novel devices such as NWSCs.

3.3 Electrical properties of Sb:SnO_2 NWs on m-, r- and a-Al_2O_3

The carrier density of the Sb:SnO_2 NWs grown on m-, r- and a-Al_2O_3 at 800 °C and 1 mbar with Sn/Sb = 0.1 was measured by the Hall effect. We obtained a carrier density of 8×10^{19} cm^{-3}

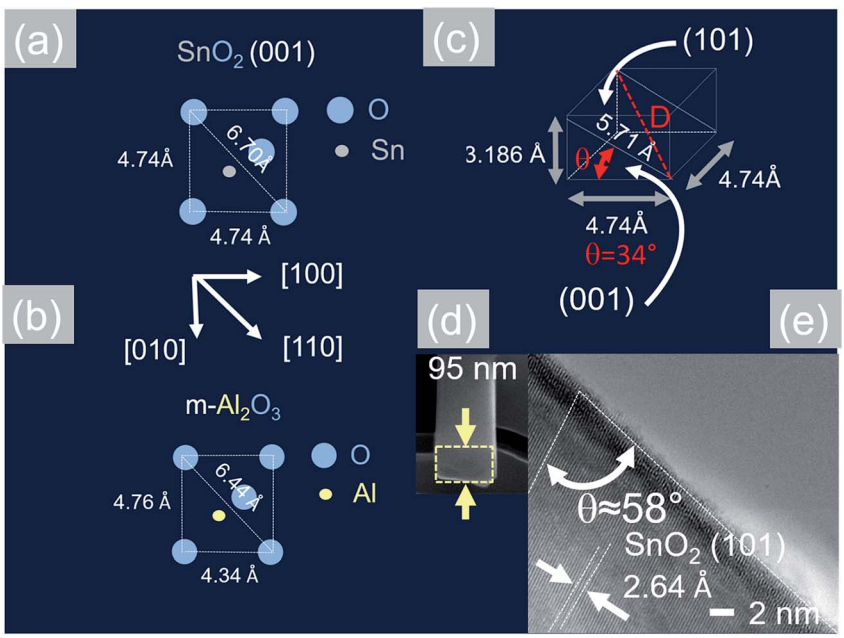

Fig. 5 (a) Two dimensional lattice of the SnO_2 (001) that is grown in an epitaxial way on (b) oxygen terminated m-Al_2O_3 (c) crystal structure of tetragonal rutile SnO_2 (d) TEM and (e) HRTEM images of a Sb:SnO_2 NW after removing it from the m-Al_2O_3.

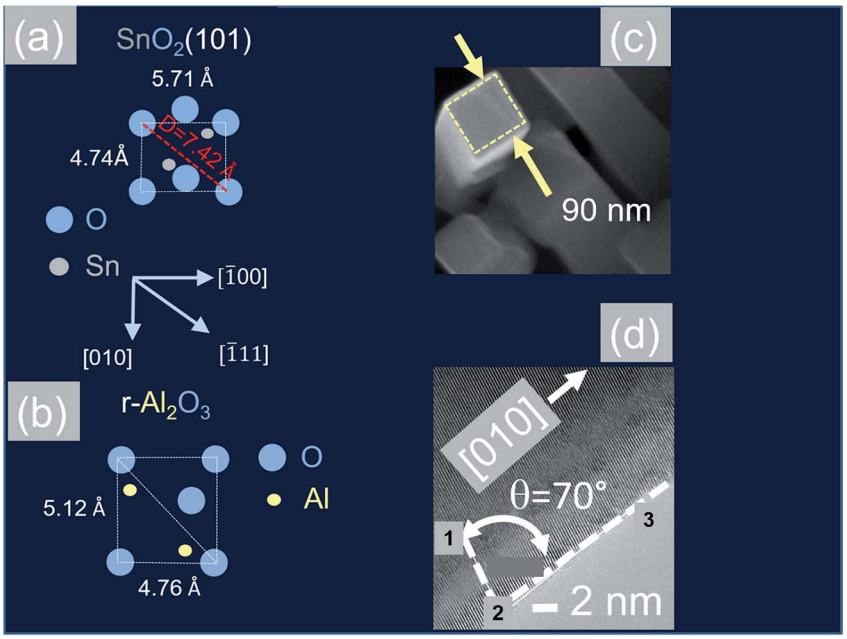

Fig. 6 (a) Two dimensional surface lattice of SnO_2 (101) which grows on (b) oxygen terminated surface of r-Al_2O_3 (c) TEM image of Sb:SnO_2 NWs after removing from r-Al_2O_3 (d) HRTEM image of the Sb:SnO_2 NWs showing the (010) lattice planes.

which is significantly larger than that measured previously in un-doped SnO_2 NWs, that was of the order of 10^{16} cm^{-3}.[33] The conductivity of the Sb:SnO_2 NWs was found to be $\approx 3 \times 10^2$ $(\Omega\ cm)^{-1}$ giving a mobility of 20 $cm^2\ V^{-1}\ s^{-1}$ which is lower compared to 70 $cm^2\ V^{-1}\ s^{-1}$ in un-doped SnO_2 NWs that was previously measured by THz conductivity spectroscopy.[33] We did not observe a significant variation in the carrier density of the Sb:SnO_2 NWs on m-, r- and a-Al_2O_3, or due to slight variations of Sn/Sb = 0.15 ± 0.05. We measured the Hall effect of the Sb:SnO_2 NWs obtained with Sn/Sb = 0.15 and found a carrier density of 8.3×10^{19} cm^{-3} which is very close to that obtained with Sn/Sb = 0.1. However the carrier density in the Sb:SnO_2 NWs obtained at 900 °C was smaller *i.e.* 6×10^{18} cm^{-3} while those obtained at 1000 °C had an even smaller carrier density of 4×10^{17} cm^{-3} and conductivity of ≈ 3 $(\Omega\ cm)^{-1}$. This is attributed to the transfer of the Sb into the gas stream during the temperature ramp, and before the onset of one dimensional growth, due to the high vapor pressure of Sb, which in turn limits the supply and incorporation of Sb impurities into the SnO_2 NWs during the growth step. This trend is consistent with

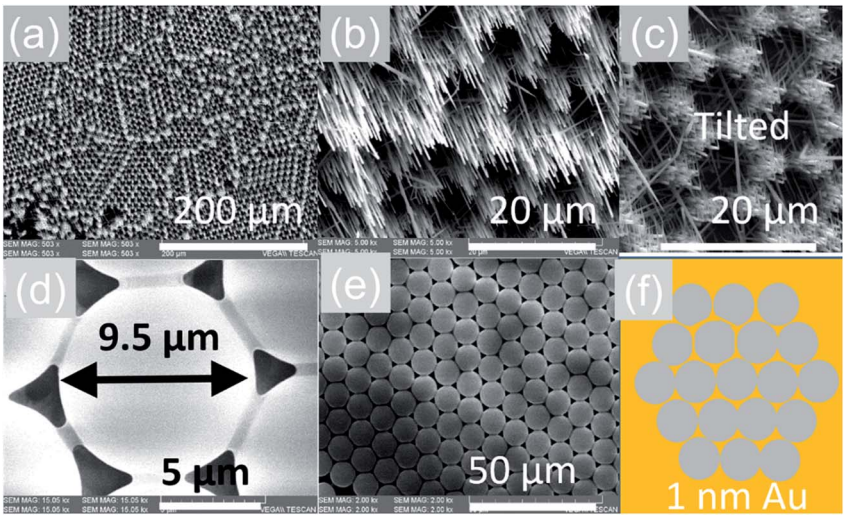

Fig. 7 Selective area location growth of Sb:SnO_2 NWs on r-Al_2O_3 (a) low magnification and (b) high magnification image (c) tilted view of the Sb:SnO_2 NWs on r-Al_2O_3 showing that they do not consist two segments as shown in Fig. 3(f); (d) an individual sphere in contact with its six closest neighbors (e) domain of ordered spheres (f) schematic representation of the spheres on r-Al_2O_3 after the deposition of 1 nm Au in between the spheres.

the findings of Klamchuen *et al.*,[22] who found that the doping level in SnO_2 NWs grown at 650 °C was twice that obtained at 750 °C, attributed to a suppression of impurity re-evaporation. They also observed that the doping level did not increase further upon reducing the growth temperature from 650 °C to 550 °C, which was explained by a suppression of the diffusion length of impurity ad-atoms on the surface of the SnO_2 NWs, and the presence of a temperature activated energy barrier which is necessary for the incorporation of the Sb impurities into the host lattice of SnO_2.

We suggest that the incorporation of Sb impurities into the SnO_2 NWs occurs through the sides of the SnO_2 NWs by thermal diffusion, or, *via* the triple phase junction, as shown in Fig. 1(c), similar to the mechanism proposed by Klamchuen *et al.*[22] This is also corroborated by the fact that we did not detect any Sb in the Au particles after attempting to grow SbO_2, Sb_2O_3 or Sb_2O_5 NWs on r-Al_2O_3, by using only Sb, and also by the fact that we did not detect any Sb in the Au:Sn particles on the ends of the Sb:SnO_2 NWs, as shown in Fig. 3(e). It is also consistent with the findings of McGinley *et al.*,[39] who showed that the surface of SnO_2 nanoparticles is terminated by an oxygen rich layer, but when doped n-type with 9% or 17% Sb, the impurity atoms are concentrated near the surface of the SnO_2 nanoparticles with an oxidation state of five.

In order to obtain a more detailed understanding of the electronic properties of the Sb:SnO_2 NWs we carried out electronic structure calculations from first principles using the CASTEP plain wave DFT code[40,41] and the Heyd–Scuseria–Ernzerhof (HSE)[42] exchange correlate-correlation energy functional. After relaxation of the cell, we obtained lattice constants of $a = b = 4.82$ Å and $c = 3.23$ Å which are in close agreement to reported values.[42] DOS calculations were performed for the case of (a) the perfect SnO_2 cell and (b) the Sb-doped SnO_2 cell, shown in Fig. 8(a) and (b) respectively. The maximum of the valence band (VB) is set at zero energy level. It is evident from the partial density of states shown in Fig. 8(a) and (b) that the VB is dominated by O and the CB by Sn.[60] The band gap was found to be 3.6 eV for the perfect structure but a slight reduction of the band gap down to 3.5 eV was observed with doping. This semi-empirical method yields a much more accurate band gap than calculations performed based on the Perdew–Burke–Ernzerhof (PBE) GGA functional which are not shown here. In addition we find that the incorporation of Sb into the SnO_2 crystal does not produce any deep levels within the band gap which are in general detrimental to the operation of optoelectronic devices such as solar cells, light emitting diodes *etc.* In other words the Sb impurities are incorporated into the SnO_2 lattice as substitutional donors and our calculations show that the Fermi level resides 0.46 eV above the CB edge for 12.5 at% Sb ($\equiv 4 \times 10^{21}$ cm^{-3}).

In addition, we calculated the conduction band (CB) potential profile, and one dimensional electron gas (1DEG) charge distribution, along the radial direction, *via* the self-consistent solution of the Poisson–Schrödinger (SCPS) equations, in the effective mass approximation, as described in detail elsewhere.[43] The SCPS calculations were carried out by taking into account the effective mass and dielectric constant of SnO_2 , *i.e.* $m_e^* = 0.3$ (ref. 44 and 45) and $\varepsilon_r = 13.5$ (ref. 46 and 47) respectively. In order to obtain a carrier density of 8×10^{19} cm^{-3} as determined from the Hall effect we have taken the Fermi level to be energetically located ≈0.3 eV above the CB edge, at the surface of the Sb:SnO_2 NWs. This is consistent with the electronic structure calculations of Mishra *et al.*,[48] who showed that the Sb impurities in SnO_2 form a band, which has an energetic overlap with the conduction band and a nearly free electron structure, *i.e.* behaves like a metallic band. It is also consistent with Li *et al.*,[49] who calculated the electronic structure of Sb:SnO_2 for 6.25% Sb, and found that the Fermi level moves into the CB upon the incorporation of Sb, and displays metallic character, but also with Farahani *et al.*,[50] who showed that the Fermi level resides ≈0.33 eV above the CB edge at the surface of Sb:SnO_2 epitaxial layers grown by molecular beam epitaxy on r-Al_2O_3.

The CB potential profile with respect to the Fermi level, *i.e.* $E_C - E_F$ and 1DEG charge distribution, *versus* distance along the radial direction of the Sb:SnO_2 NWs, is shown in Fig. 8(d), where we have taken the donor impurities to be confined between $r =$ 20 and 40 nm. The CB edge potential profile is near flat band in the vicinity of the core and the 1DEG charge distribution has a maximum at the core and a local maximum at the surface. It should be noted that we obtain similar band profiles and charge distributions by taking a uniform distribution of Sb impurities throughout the Sb:SnO_2 NWs. However the 1DEG in the vicinity of the core is expected to have a higher mobility when the density of donor impurities is larger at the surface than the core, as is the case in Fig. 9(d). In other words, the incorporation of Sb impurities into the SnO_2 NWs *via* surface diffusion is not a drawback in the end. We estimate that the mobility in the Sb:SnO_2 NWs with a maximum carrier density of the order of 10^{20} cm^{-3} is a few tens of cm^2 V^{-1} s^{-1} (ref. 23 and 24) so the resistivity of the Sb:SnO_2 NWs is of the order of 10^{-3} Ω cm which in turn is attractive for the deposition of metal contacts with low resistance and the fabrication of high performance devices.

3.4 Optical properties of Sb:SnO_2 NWs on m-, r- and a-Al_2O_3

In the past the transmission of light through Sb:SnO_2 NWs[14–24] has not been investigated as they were not ordered or oriented along any particular direction which in turn leads to a considerable suppression of transmission and transparency. In contrast a higher transmission of light is expected to occur through ordered MO NWs. We measured the steady state transmission through the Sb:SnO_2 NWs that were grown at 800 °C on r-Al_2O_3 as shown in Fig. 9(d). The Sb:SnO_2 NWs have an optical transmission of 80% above 800 nm but they absorb light in the visible between 400 nm to 800 nm. We do not observe any interference effects since the spacing between the Sb:SnO_2 NWs is considerably smaller than the wavelength of light. In addition we find that the Sb:SnO_2 NWs on r-Al_2O_3 obtained at 900 °C and 1000 °C have a higher transparency compared to those obtained at 800 °C due to their shorter lengths. In order to understand the origin of the absorption we have measured the transient absorption through the Sb:SnO_2 NWs on an fs time scale as shown in Fig. 9(a)–(c). In all cases, we

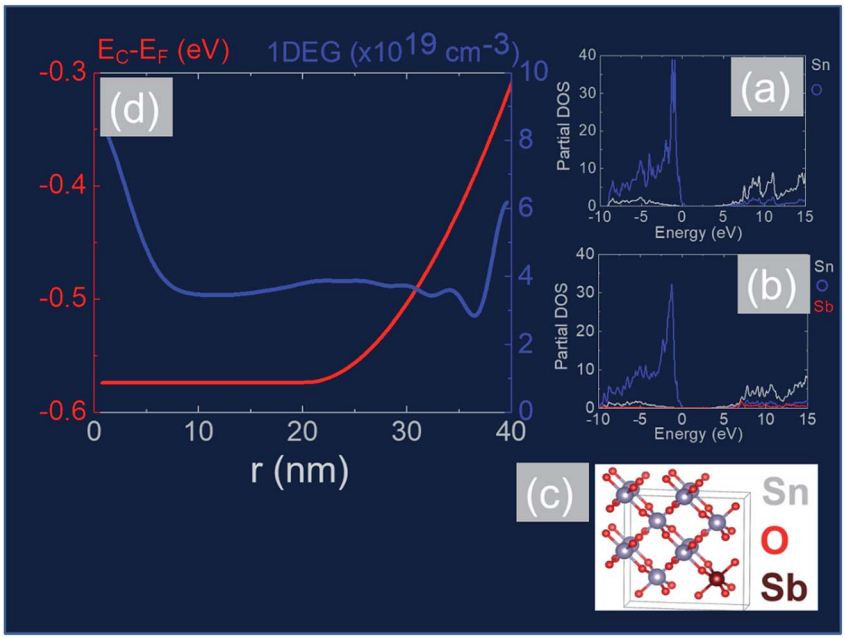

Fig. 8 (a) DOS for un-doped SnO_2 and (b) DOS for Sb:SnO_2 with 12.5 at% ($\equiv 4 \times 10^{21}$ cm^{-3}) (c) structural model showing Sb substitutional donor impurity in SnO_2 (d) SCPS CB potential profile (red) and 1DEG charge distribution (blue) *versus* distance along the radial direction of a Sb:SnO_2 NWs with a diameter of 80 nm taking $E_C - E_F = -0.3$ eV at the surface and assuming a uniform distribution of ionized donor impurities $N_D^+ = 1 \times 10^{19}$ cm^{-3} between $r = 20$ and 40 nm.

observe a strong peak in the time evolution of the differential absorption between 500 nm and 600 nm attributed to the surface plasmon resonance (SPR) of the Au–Sn particles, corresponding to sizes between 10 nm and 100 nm (ref. 51) and the existence of surface states lying energetically in the energy gap of SnO_2.[52] One may observe a slight blue shift of the peak from 900 °C to 1000 °C in Fig. 9(b) and (c), consistent with that observed in the steady state transmission, that might be related to the smaller size of the Au–Sn particles due to the depletion of Sn that occurs during the temperature ramp and/or the elimination of mid gap states at elevated temperatures. It is important to point out, that the transparency of the Sb:SnO_2 NWs on r-

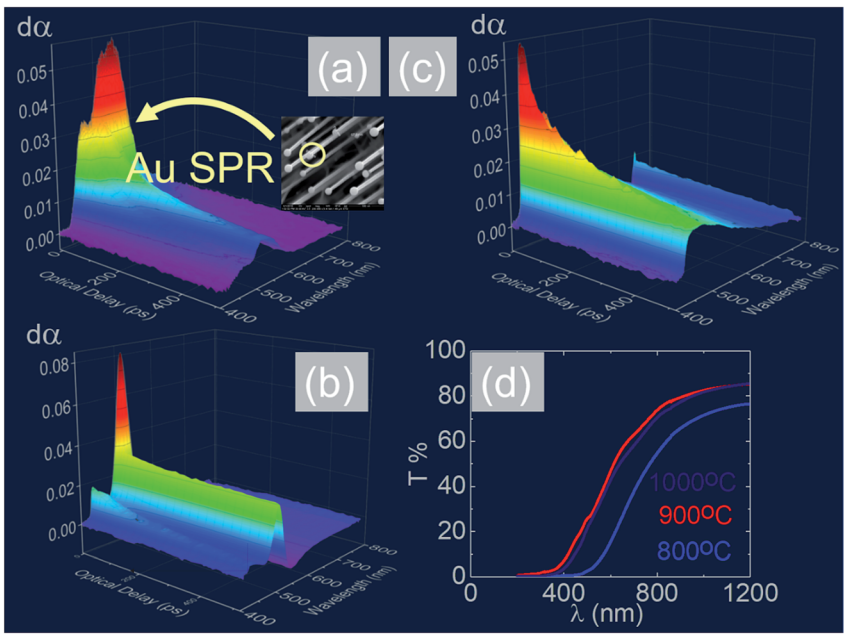

Fig. 9 Ultrafast, differential transient absorption dα *versus* optical delay τ (ps) and probe wavelength λ (nm) through the Sb:SnO_2 NWs grown on r-Al_2O_3 at (a) 800 °C, (b) 900 °C and (c) 1000 °C; (d) steady state transmission of light through the Sb:SnO_2 NWs grown on r-Al_2O_3 at different temperatures.

Al_2O_3 may be increased further by selective area location growth as shown in Fig. 7 which leads to a higher transmission through the voids between the Sb:SnO_2 NW.

Finally it is worthwhile considering the PL obtained from the Sb:SnO_2 NWs, grown on r-Al_2O_3 at 800 °C, as shown in Fig. 10(a), in which case we observe emission at $\lambda = 600$ nm ($\equiv$2.1 eV) and 300 K. Bulk SnO_2 has a direct energy band gap of 3.7 eV but the even – parity symmetry of the conduction-band minimum and valence-band maximum states prohibits band – edge radiative transitions which has limited the use of SnO_2 for the fabrication of light emitting diodes. The PL at 2.1 eV is attributed to radiative recombination between deep donor and acceptor like states residing energetically in the energy band gap of SnO_2 that are related to oxygen vacancies. We observe a suppression of the maximum at $\lambda = 600$ nm and the emergence of emission at $\lambda =$ 470 nm ($\equiv$2.6 eV) by decreasing the temperature from 300 K to 10 K due to radiative recombination *via* shallower levels as proposed by Luo *et al.*[53] However an interesting aspect of the PL emission at 2.1 eV and 2.6 eV is that it has a lifetime of $\tau \approx 0.2$ ms as shown by the time resolved PL in Fig. 10(b). This is considerably higher than the lifetimes extracted from SnO_2 rods and particles which are of the order of 100 ns (ref. 54) and comparable to Eu doped SnO_2 nanocrystals.[55] Hence, in principle, the Sb:SnO_2 NWs described here may be processed into devices capable of light emission but also NWSCs.[56,57]

To the best of our knowledge no one has previously used ordered networks of Sn:In_2O_3 or Sb:SnO_2 NWs to make NWSCs despite the fact that Battaglia *et al.*[58] has showed that periodic photonic nanostructures outperform their random counterparts in trapping light in solar cells. It is desirable then to use these highly conductive, ordered networks, of Sb:SnO_2 NWs in order to improve the performance of all-solid state NWSCs. In addition the Sb:SnO_2 NWs can be used in perovskite solar cells as an electron transport layer (ETL). According to Jiang *et al.*[59] a traditional ETL such as TiO_2, is not very efficient for charge extraction at the interface, especially in planar structures. In addition, the devices using TiO_2 suffer from serious degradation under ultraviolet illumination. SnO_2 shows a better band alignment with the perovskite absorption layer and higher electron mobility, which is helpful for electron extraction. Consequently the specific ordered networks of Sb:SnO_2 NWs described here may serve as a scaffold on top of which one may deposit a perovskite absorber layer and a hole transport layer in order to create a p–n junction solar cell.

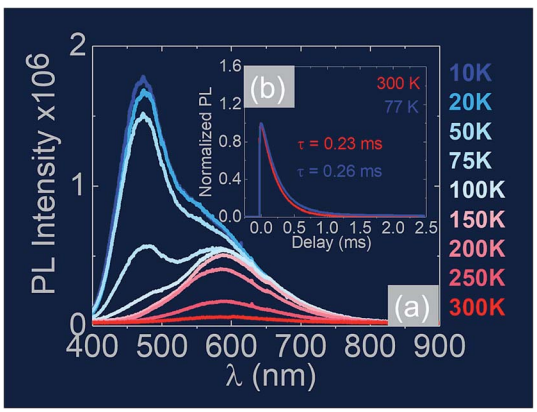

Fig. 10 (a) Temperature dependence of the PL obtained from the Sb:SnO_2 NWs grown on r-Al_2O_3 at 800 °C (b) time resolved PL taken at $\lambda = 600$ nm for 300 K and 77 K along with the corresponding lifetimes.

4 Conclusions

We have grown epitaxial, ordered Sb:SnO_2 NWs *via* the VLS mechanism on m-, r- and a-Al_2O_3 between 700 °C and 1000 °C using metallic Sn containing an excess of Sb *i.e.* for Sn/Sb = 0.15 ± 0.05 under a flow of Ar and O_2 at 1.5 ± 0.5 mbar. One dimensional growth was suppressed for Sn/Sb < 0.1 while the Sb:SnO_2 NWs were not oriented along any particular direction for Sn/Sb > 0.2. Consequently highly conductive and directional Sb:SnO_2 NWs may only be obtained in a narrow window of growth conditions. All of the Sb:SnO_2 NWs have the tetragonal rutile crystal structure and square sections. The Sb:SnO_2 NWs are oriented along two mutually perpendicular directions forming a rectangular mesh on m-Al_2O_3 with a maximum lattice mismatch of 0.1%. In contrast the Sb:SnO_2 NWs on r-Al_2O_3 are all oriented in one direction but have a larger lattice mismatch of 10%. The morphology and growth directions of the Sb:SnO_2 NWs on m-, r- and a-Al_2O_3 did not change by varying the growth temperature between 700 °C and 1000 °C but the carrier density changed from 8×10^{19} cm^{-3} to 4×10^{17} cm^{-3} due to the re-evaporation and limited incorporation of Sb donor impurities into the SnO_2 NWs with increasing temperature. All of the Sb:SnO_2 NWs had a high transmission of 80% above 800 nm and absorbed light between 400 nm to 800 nm primarily due to the SPR of the Au particles. The transmission may be improved significantly by selective area location growth which we have shown that is possible on r-Al_2O_3 by patterning the catalyst. In addition the Sb:SnO_2 NWs on m-, r- and a-Al_2O_3 are capable of light emission with remarkably long lifetimes of 0.2 ms and are attractive for the realization of NWSCs.

Conflicts of interest

There are no conflicts of interest to declare.

References

1 Q. Wan, E. N. Dattoli and W. Lu, *Appl. Phys. Lett.*, 2007, **90**, 222107.
2 M. Zervos, C. Mihailescu, J. Giapintzakis, C. Luculescu, N. Florini, P. Komninou, J. Kioseoglou and A. Othonos, *APL Mater.*, 2014, **2**, 056104.
3 S. N. Bai, H. H. Tsai and T. Y. Tseng, *Thin Solid Films*, 2007, **516**, 155.
4 H. Duan, H. He, L. Sun, S. Song and Z. Ye, *Nanoscale Res. Lett.*, 2013, **8**(1), 493.
5 C. O. Dwyer, M. Szachowicz, G. Visimberga, V. Lavayen, S. B. Newcomb and C. M. S. Torres, *Nat. Nanotechnol.*, 2009, **4**, 239.

6 J. Gao, R. Chen, D. H. Li, L. Jiang, J. C. Ye, X. C. Ma, X. D. Chen, Q. H. Xiong, H. D. Sun and T. Wu, *Nanotechnology*, 2011, **22**, 195706.
7 Q. Wan, E. N. Dattoli, W. Y. Fung, W. Guo, Y. Chen, X. Pan and W. Lu, *Nano Lett.*, 2006, **6**, 2909, DOI: 10.1021/nl062213d.
8 P. Nguyen, H. T. Ng, J. Kong, A. M. Cassell, R. Quinn, J. Li, J. Han, M. McNeil and M. Meyyappan, *Nano Lett.*, 2003, **3**, 925.
9 D. Tsokkou, A. Othonos and M. Zervos, *Appl. Phys. Lett.*, 2012, **100**, 133101.
10 Q. Wan, E. Dattoli and W. Lu, *Small*, 2008, **4**, 451.
11 Z. H. Luo, D. S. Tang, H. Kuo, Y. Fang, Y. Q. Chen, X. W. He, Y. H. Peng, H. J. Yuan and Y. Yang, *Chin. Phys. B*, 2010, **19**, 026102.
12 C. Amorim, C. Dalmaschio, E. Leite and A. Chiquito, *J. Phys. D: Appl. Phys.*, 2014, **47**, 045301.
13 F. Ma, Y. Jiao, G. Gao, Y. Gu, A. Bilic, S. Sanvito and A. Du, *ACS Appl. Mater. Interfaces*, 2016, **8**, 25667.
14 Q. Wan and T. H. Wang, *Chem. Commun.*, 2005, **30**, 3841.
15 L. Li, J. Huang, T. Wang, H. Zhang, Y. Liu and J. Li, *Biosens. Bioelectron.*, 2010, **25**, 2436.
16 X. Rui-Jie and L. Hui-Xuan, *Chin. Phys. B*, 2012, **21**, 088104.
17 Q. Wan, J. Huang, Z. Xie, T. Wang, E. N. Dattoli and W. Lu, *Appl. Phys. Lett.*, 2008, **92**, 102101.
18 J. Huang, A. Lu, B. Zhao and Q. Wan, *Appl. Phys. Lett.*, 2007, **91**, 073102.
19 B. R. Sathe, M. Patil, P. S. Walke, J. P. Vivek, A. Lele, V. K. Pillai and I. S. Mulla, *Sci. Adv. Mater.*, 2009, **1**, 38.
20 S. T. Jean and Y. C. Her, *J. Appl. Phys.*, 2009, **105**, 024310.
21 R. Kumar, K. Rao, K. Rajanna and A. Phani, *Mater. Lett.*, 2013, **106**, 164.
22 A. Klamchuen, T. Yanagida, K. Nagashima, S. Seki, K. Oka, M. Taniguchi and T. Kawai, *Appl. Phys. Lett.*, 2009, **95**, 053105.
23 I. Costa, Y. Colmenares, P. Pizani, E. Leite and A. Chiquito, *Chem. Phys. Lett.*, 2018, **695**, 125.
24 I. Costa, E. Bernardo, B. Marangoni, E. Leite and A. Chiquito, *J. Appl. Phys.*, 2016, **120**, 225109.
25 S. Mathur and S. Barth, *Small*, 2007, **3**, 2070.
26 W. S. Kim, D. Kim, K. L. Choi, J. G. Park and S. H. Hong, *Cryst. Growth Des.*, 2010, **10**, 4747.
27 A. Leonardy, W. Z. Hung, D. S. Tsai, C. C. Chou and Y. S. Huang, *Cryst. Growth Des.*, 2009, **9**, 3958.
28 L. Mazeina, Y. N. Picard, J. D. Caldwell, E. R. Glaser and S. M. Prokes, *J. Cryst. Growth*, 2009, **311**, 3158.
29 W. S. Kim, D. Kim and S. H. Hong, *CrystEngComm*, 2014, **16**, 9340.
30 Y. H. Choi, J. Na, J. S. Kim, M. K. Joo, G. T. Kim and P. S. Kang, *J. Korean Phys. Soc.*, 2014, **65**, 502.
31 X. Wang, N. Aroonyadet, Y. Zhang, M. Mecklenburg, X. Fang, H. Chen, E. Goo and C. Zhou, *Nano Lett.*, 2014, **14**, 3014.
32 E. P. Stuckert, R. H. Geiss, C. J. Miller and E. R. Fisher, *ACS Appl. Mater. Interfaces*, 2016, **8**, 22345.
33 D. Tsokkou, A. Othonos and M. Zervos, *Appl. Phys. Lett.*, 2012, **100**, 133101.
34 M. Zervos, A. Othonos, E. Tanasa and E. Vasile, *J. Phys. Chem. C*, 2018, **122**, 22709.
35 D. Tsivion, M. Schvartzman, R. Popovitz-Biro and E. Joselevich, *ACS Nano*, 2012, **6**, 6433.
36 R. A. Hughes, E. Menumerov and S. Neretina, *Nanotechnology*, 2017, **28**, 282002.
37 A. L. Giermann and C. V. Thompson, *Appl. Phys. Lett.*, 2005, **86**, 121903.
38 W. S. Kim, D. H. Kim, Y. G. Jang and S. H. Hong, *CrystEngComm*, 2012, **14**, 1545.
39 C. McGinley, S. A. Moussalami, M. Riedler, M. Pflughoe, H. Borchert, M. Haase, A. R. B. Castro, H. Weller and T. Möller, *Eur. Phys. J. D*, 2001, **16**, 225.
40 M. D. Segall, P. J. D Lindan, M. J. Probert, C. J. Pickard, P. J. Hasnip, S. J. Clark and M. C. Payne, *J. Phys.: Condens. Matter*, 2002, **14**, 2717.
41 S. J. Clark, M. D. Segall, C. J. Pickard, P. J. Hasnip, M. J. Probert, K. Refson and M. C. Payne, *Z. Kristallogr.*, 2005, **220**, 567.
42 W. Korner, D. F. Urban, D. M. Ramo, P. D. Bristowe and C. Elsasser, *Phys. Rev. B: Condens. Matter Mater. Phys.*, 2014, **90**, 195142.
43 M. Zervos and L. F. Feiner, *J. Appl. Phys.*, 2004, **95**, 1.
44 K. J. Button, C. G. Fonstad and W. Debrodt, *Phys. Rev. B: Solid State*, 1971, **4**, 4539.
45 Y. Mi, H. Odaka and S. Iwata, *Jpn. J. Appl. Phys., Part 1*, 1999, **38**, 3453.
46 H. J. Daal, *J. Appl. Phys.*, 1968, **39**, 4467.
47 M. Batzill and U. Diebold, *Prog. Surf. Sci.*, 2005, **79**, 47.
48 K. C. Mishra, K. H. Johnson and P. C. Schmidt, *Phys. Rev. B: Condens. Matter Mater. Phys.*, 1995, **51**, 13972.
49 Z. Q. Li, Y. L. Yin, X. D. Liu, L. Y. Li, H. Liu and Q. G. Song, *J. Appl. Phys.*, 2009, **106**, 083701.
50 S. Farahani, T. Veal, J. Mudd, D. Scanlon, G. Watson, O. Bierwagen, M. White, J. Speck and C. McConville, *Phys. Rev. B: Condens. Matter Mater. Phys.*, 2014, **90**, 155413.
51 S. Link and M. El-Sayed, *J. Phys. Chem. B*, 1999, **103**, 4212.
52 A. Othonos, M. Zervos and D. Tsokkou, *Nanoscale Res. Lett.*, 2009, **4**, 828.
53 S. Luo, P. K. Chu, W. Liu, M. Zhang and C. Lin, *Appl. Phys. Lett.*, 2006, **88**, 183112.
54 A. Kar, S. Kundu and A. Patra, *J. Phys. Chem. C*, 2011, **115**, 118.
55 A. Kar and A. Patra, *J. Phys. Chem. C*, 2009, **113**, 4375.
56 M. Zervos, E. Vasile, E. Vasile, E. Karageorgou and A. Othonos, *J. Phys. Chem. C*, 2016, **120**, 11.
57 E. Karageorgou, M. Zervos and A. Othonos, *APL Mater.*, 2014, **2**, 116107.
58 C. Battaglia, C. M. Hsu, K. Soderstrom, J. Escarre, F. J. Haug, M. Charriere, M. Boccard, M. Despeisse, D. T. L. Alexander, M. Cantoni, Y. Cui and C. Ballif, *ACS Nano*, 2012, **6**, 2790.
59 Q. Jiang, X. Zhang and J. You, *Small*, 2018, **14**, 1801154.
60 J. Robertson, *J. Phys. C: Solid State Phys.*, 1979, **12**, 4767.

